Electronic Supplementary Information

Stable Methylammonium-Intercalated 1T'-MoS_2 for Efficient Electrocatalytic Hydrogen Evolution

In Hye Kwak,[a] *Ik Seon Kwon*,[a] *Hafiz Ghulam Abbas,*[b] *Gabin Jung*,[a] *Yeron Lee*,[a] *Jeunghee Park,**[,a] *and Hong Seok Kang**[,c]

[a] Department of Chemistry, Korea University, Sejong 339-700, Korea,
E-mail: parkjh@korea.ac.kr

[b] Department of Nanoscience and Nanotechnology, Jeonbuk National University, Chonju, Chonbuk 560-756, Korea.

[c] Department of Nano and Advanced Materials, College of Engineering, Jeonju University, Chonju, Chonbuk 560-759, Korea, E-mail: hsk@jj.ac.kr

Contents

Table S8. Closest distance of N-N in the intercalated complexes.

III. Supplementary Figures

Fig. S1 SEM images.

Fig. S2 NMR data.

Fig. S3 IR spectrum data.

Fig. S4 XRD data.

Fig. S5 XANES and EXAFS data.

Fig. S6 XPS data.

Fig. S7 XPS valence spectrum data.

Fig. S8 Raman spectrum data.

Fig. S9 TGA and DSC data.

Fig. S10 Chronoamperometric responses of HER using the Pt and graphite rod as a counter electrode

Fig. S11 Nyquist plots.

Fig. S12 Cyclic voltammograms for evaluation of double-layer capacitance.

Fig. S13 Computed structures of (4×4) MoS_2-*m*NH_4 and (4×4) MoS_2-*m*CH_3NH_3.

Fig. S14 Relative energies of the 1T' and 2H phases (4×4) MoS_2 vs. C_{Vs}.

Fig. S15 $\Delta q(z)$ and $\Delta Q(z)$ data.

Fig. S16 Contour plots of $\Delta\rho(x, y, z)$.

IV. References

I. Experimental

Synthesis. MoS_2 nanostructures were synthesized using a hydrothermal decomposition reaction of $(NH_4)_2MoS_4$; (i) $(NH_4)_2MoS_4 \rightarrow MoS_3+2NH_3+H_2S$; (ii) $MoS_3 \rightarrow MoS_2 + S$.[S1] $(NH_4)_2MoS_4$ (0.254 mmol, 66 mg) was dissolved in deionized water (10 mL). Then, 0.125-1.25 mmol of ammonium chloride (NH_4Cl) or methyl ammine hydrochloride ($CH_3NH_2{\cdot}HCl$) was added to synthesize the intercalated structures. The reaction mixture was transferred to a Teflon-lined stainless-steel autoclave. A hydrothermal reaction was performed at 180–220 °C for 12 h in an electric oven. The product was collected by centrifugation, washed thoroughly with deionized water and acetone several times, and then vacuum-dried at room temperature.

Characterization. The products were characterized by scanning electron microscopy (SEM, Hitachi S-4700), and field-emission transmission electron microscopy (FE TEM, FEI TECNAI G2 200 kV, Jeol JEM 2100F, HVEM). Energy-dispersive X-ray fluorescence spectroscopy (EDX) with elemental maps was measured using a TEM (FEI Talos F200X) operated at 200 keV that equipped with high-brightness Schottky field emission electron source (X-FEG) and Super-X EDS detector system (Bruker Super-X). This EDX has powerful sensitivity and resolution in the low photon energy region. Fast Fourier-transform (FFT) images were generated by the inversion of the TEM images using Digital Micrograph GMS1.4 software (Gatan Inc.). High-resolution X-ray diffraction (XRD) patterns were obtained using the 9B and 3D beamlines of the Pohang Light Source (PLS) with monochromatic radiation (λ = 1.54595 Å). XRD pattern measurements were also carried out in a Rigaku D/MAX-2500 V/PC using Cu K_α radiation (λ = 1.54056 Å). XPS data were collected using the 8A1 beam line of the PLS with a photon energy of 600 or 640 eV

X-ray absorption near edge spectra (XANES) and extended X-ray absorption fine structure (EXAFS) spectra at the Mo K-edge were collected in transmission mode using the 10C beam line of the PLS with a ring current of 350 mA at 3.0 GeV. Energy calibration was carried out by simultaneously measuring the reference spectrum of Mo metal foil. Least-squares fits of EXAFS data were performed using the Athena and Artemis software packages, version 0.9.25.

The solid-state ^{13}C (100.64 MHz) NMR spectra were acquired on a Bruker AVANCE II^{+} 400 MHz NMR system (at the KBSI Seoul Western Center) equipped with a Bruker 3.2 mm bore HXY probe operating in HX mode. The magic angle spinning ^{13}C NMR experiments (one pulse method) were performed using a pulse length of 2 μs for a $\pi/2$ pulse length of 5 μs, and a pulse repetition delay time of 5 s. The spectra were referenced to an external adamantane standard in which the peak at higher chemical shift was set at 38.43 ppm. The spectra were processed using the Bruker Topspin software (version 3.2) using conventional techniques, and a 50 Hz line broadening window function was applied in all cases.

Attenuated total reflectance Fourier transform infrared (ATR FTIR) spectra were obtained on on a LabRam ARAMIS IR^2 (HORIBA JOBIN YVON). Spectra were collected by pressing the sample onto a diamond crystal with a pressure setting of 90 on the DuraScope. Each spectrum consisted of 16 spectra co-added accumulated between 4000 cm^{-1} and 560 cm^{-1} with a spectral resolution of 4 cm^{-1}.

Thermogravimetric analysis (TGA) and differential scanning calorimetry (DSC) measurements were performed using a Differential Scanning Calorimeter/Thermal Analyzer (Perkin Elmer DSC8000, Pyris 1TGA). The samples (10 mg) were heated from room temperature to 700 °C in a N_2 flow (100 sccm), at 10 °C/min. Elemental analyses were

performed on a ThermoFisher Flash EA2000 analyzer. Raman spectra were measured with a micro-Raman spectrometer (Horiba ARAMIS IR^2), using a diode laser with an excitation wavelength of 532 nm.

Electrochemical Measurements. HER electrocatalysis (in 0.5 M H_2SO_4 electrolyte) was measured using a linear sweeping from 0 to -0.8 V (vs. RHE) with a scan rate of 2 mV s^{-1}. A saturated calomel electrode (SCE) was used as reference electrode, and a Pt wire was used as counter electrode. The electrolyte was purged with H_2 (ultrahigh grade purity) during the measurement. The applied potentials (E) reported in our work were referenced to the reversible hydrogen electrode (RHE) through standard calibration. In 0.5 M H_2SO_4 electrolyte (pH 0), E (vs. RHE) = E (vs. SCE) + E_{SCE} (= 0.241 V) + 0.0592 pH = E (vs. SCE) + 0.241 V. The overpotential (η) was defined as E (vs. RHE). 4 mg MS sample was mixed with 2 mg carbon black (Vulcan XC-72) dispersed in Nafion (20 μL) and isopropyl alcohol (0.98 mL). The catalyst materials (0.39 mg cm^{-2}) were deposited on a glassy carbon rotating disk electrode (RDE), and a rotation speed of 1600 rpm was used for the linear sweep voltammetry (LSV) measurements.

Electrochemical impedance spectroscopy (EIS) measurements were carried out for the electrode in an electrolyte by applying an AC voltage of 10 mV in the frequency range of 100 kHz to 0.1 Hz at a bias voltage of -0.15 V (vs. RHE). To measure double-layer capacitance via CV, a potential range in which no apparent Faradaic processes occur was determined from static CV. This range is 0.1–0.2 V. All measured current in this non-Faradaic potential region is assumed to be due to double-layer capacitance. The charging current, i_c, is then measured from CVs at multiple scan rates. The working electrode was held at each potential vertex for 10 s before beginning the next sweep. The double-layer capacitance current density (J) is equal

to the product of the scan rate (ν) and the electrochemical double-layer capacitance (C_{dl}), as given by equation $J = \nu C_{dl}$, Thus, a plot of J as a function of ν yields a straight line with a slope equal to C_{dl}. The scan rates were 20–200 mV s^{-1}.

Computations. Geometry optimizations were performed using the Vienna ab-initio simulation package (VASP).[S2,S3] The electron-ion interactions were described using the projector-augmented wave (PAW) method, which is primarily a frozen-core all-electron calculation.[S4] Attractive van der Waals interactions were included using Grimme's correction for the PBE-D3 method.[S5] For structure optimization, atoms were relaxed in the direction of the Hellmann-Feynman force using the conjugate gradient method with an energy cut-off of 520 eV until a stringent convergence criterion (of 0.02 eV/Å) was satisfied. Lattice constants are optimized using the PBE-D3 exchange-correlation functional. The *k*-point sampling was performed using Γ-centered 8×8×4 points, which gives the total energy of a (4×4) MoS_2 complex within 1 meV.

II. Supporting Tables

Table S1. Composition (mole %) of samples determined by elemental analysis.

Sample[a]	Temp. (°C)[a]	[H]	[C]	[N]	[S]	[O]	[A or MA]/MoS_2 [b]
MS-0	220	30.9	2.8	0.5	44.6	21.2	2.2%
MS-A	200	37.4	4.9	2.6	37.8	17.3	14%
MS-MA	200	38.3	10.5	2.7	38.1	10.4	14%

[a] Synthesis temperature; [b] The ratio calculated using the ratio of 2 × [N]/[S].

Table S2. Fitting parameters of EXAFS data for the MoS_2 samples (see Figure S4).

Sample	Scattering Path	R (Å)[a]	CN[b]	ΔE (eV)[c]	σ^2 (Å^2)[d]
MS-0	Mo-S	2.40	6.2	2.7	0.0028
	Mo-Mo	3.16	4.2	2.6	0.0036
MS-A	Mo-S	2.41	5.7	-1.4	0.0080
	Mo-Mo	2.76	1.9	-2.0	0.0072
MS-MA	Mo-S	2.40	5.0	-1.4	0.0078
	Mo-Mo	2.76	1.7	-2.0	0.0091

[a] Distance between scattering atoms.
[b] Coordination number of Mo atoms.
[c] Edge energy shift, representing between the energy grids of experimental and theoretical data.
[d] Debye-Waller factor.

Table S3. Impedance parameters for the equivalent circuit that was shown in Figure S11, and the double-layer capacitance (C_{dl}) as shown in Figure S12.

`	EIS		C_{dl} (mF cm^{-2})
Samples	R_s (Ω)	R_{ct} (Ω)	
MS-0	6.9	910.8	18.6
MS-A	6.4	40.9	43.6
MS-MA	6.3	32.7	61.7

Table S4. Comparison of HER performance (in pH 0) of MoS_2 (with no carbon support at pH 0) in the literatures (N/A: Not applicable).

Reference	Materials	Phase	$E_{J=10}$ (mV) at 10 mA cm^{-2}	Tafel slope (mV dec^{-1})
S6	Defect-rich MoS_2 nanosheet	2H	190	50
S7	Conducting MoS_2	1T	200	40
S8	Oxygen-Incorporated MoS_2	2H	187	55
S9	Edge-terminated MoS_2 nanosheet	2H	149	49
S10	Strained MoS_2 nanosheet	2H	170	60
S11	Ammoniated MoS_2	1T	320	45
S12	1T MoS_2 single-layer nanosheets	1T	N/A	45
S13	Metallic phase MoS_2 nanosheet	1T	175	41
S14	1T MoS_2 nanosheet	1T	154	43
S15	Ammonia-MoS_2	N/A	200	55
S16	ALD-MoS_2	2H	N/A	79
S17	1T' MoS_2 monolayer	1T'	300	83
S18	1T/2H MoS_2	1T/2H	234	46
S19	Zn- MoS_2	2H	N/A	51
S20	Functionalized metallic MoS_2 nanosheet	1T	348	75
S21	1T MoS_2 nanodot	1T	173	53
Present work	MA-intercalated MoS_2 (MS-MA)	1T'	160	38

Table S5. Lattice parameters (*a, b* and *c*) of various configurations of the (4×4) MoS_2 in the 1T′ (and 1T, 1T") and 2H phases with a different number of S vacancies (N_{Vs}), and the relative energy (E_{rel}).

N_{Vs} (C_{Vs})[a]	Phase	Configurations	*a, b, c* (Å), and γ[b]	l_{Mo-Mo} (Å)[c]	E_{rel} (eV)[d]
0	2H	A_0	12.64, 12.64, 12.53, 120° (3.16)	3.16, 3.16	0.00
	1T	A_0	12.56, 12.56, 12.53, 120° (3.14)	3.17, 3.17	26.77
	1T'	A_0	13.10, 12.72, 12.52, 119° (6.55, 3.18)	2.77, 3.18	18.47
	1T"	A_0	12.88, 12.88, 12.52, 119.5° (6.44)	2.78, 3.23	20.01
8 (12.5)	2H	A_8	12.68, 12.68, 12.53, 120° (3.17)	3.16, 3.16	0.00
		B_8	12.68, 12.68, 12.53, 120° (3.17)	3.16, 3.16	0.25
	1T'	A_8	12.96, 12.68, 12.91, 119° (6.48, 317)	2.78, 3.19	9.51
		B_8	12.96, 12.68, 12.91, 119° (6.48, 3.17)	2.78, 3.19	10.96

[a] The numbers of S vacancies and the values in parentheses denote the concentration of S vacancies (C_{Vs}).
[b] Lattice constants of a 4×4 supercell configuration. The lattice constant *a* (= *b*) of the 2H and 1T" phase unit cell (shown in parentheses) was calculated as *a*/4 and *a*/2, respectively. The lattice constants *a* and *b* of the 1T' phase unit cell (also shown in parentheses) were calculated as *a*/2 and *b*/4, respectively. The angles (γ) between the *a* and *b* axes are also shown.
[c] Two shortest distances between Mo and Mo atoms. A large variation occurs for $N_{Vs} = 8$.
[d] Relative energy, defined as the total energy of each configuration minus that of the most stable configuration A_i.

In the case of the 1T' phase, the structure optimizations involved three steps. In the first step, the *a* (= *b*) and *c* constants were optimized assuming that MoS_2 adopted the 1T phase. We considered more than three configurations in which the S vacancies are distributed in different ways. In the following, the most stable configuration is labeled A_i and the other is denoted B_i, in order of stability. The second step involved further optimizations to allow all lattice parameters (including the angles) to relax freely, in such a way to minimize both forces and stresses under a restriction of $a = b$, resulting in the 1T" phase. In the last step, the lattice constants ($a \neq b$) were manually adjusted until optimal values were obtained. The final result is that all configurations adopt the 1T' phase. We do not find any case that the stability order between A_i and B_i is altered after the last two steps.

Table S6. Lattice constant of (4×4) MoS_2-$m$$NH_4$ and (4×4) MoS_2-$m$$CH_3NH_3$ complexes in the 2H and 1T' phase for various concentration (C) of NH_4 and CH_3NH_3.

Guest	m	C (%)	C_{Vs}[a]	2H	1T'
				a, c (Å)[b]	a, b, c (Å)[c]
None	0	0	0	12.64, 12.53	13.04, 12.72, 12.90
A (NH_4)	2	6.25	0	12.64, 18.00	13.06, 12.72, 17.00
	4	12.5	0	12.64, 18.00	13.04, 12.72, 17.00
	6	18.75	0	12.64, 18.30	13.04, 12.68, 17.26
	8	25	0	12.64, 18.20	13.04, 12.68, 17.26
	10	31.25	0	12.64, 18.50	13.04, 12.68, 17.30
	12	37.5	0	12.64, 18.50	12.96, 12.68, 17.50
MA (CH_3NH_3)	2	6.25	0	12.64, 18.40	13.04, 12.72, 17.80
	4	12.5	0	12.64, 18.40	13.04, 12.72, 18.00
	6	18.75	0	12.64, 18.60	13.04, 12.72, 18.23
	8	25	0	12.64, 19.00	13.12, 12.85, 17.97
	10	31.25	0	12.64, 19.50	13.14, 12.81, 18.24
	12	37.5		12.64, 19.50	13.14, 12.81, 18.24
None (N_{Vs}= 8)[d]	0	0	12.5	12.68, 12.53	12.96, 12.68, 12.91
MA (N_{Vs}= 8) [d]	2	6.25	12.5	12.68, 18.00	12.96, 12.68, 17.50
	4	12.5	12.5	12.68, 18.20	12.96, 12.68, 17.80
	6	18.75	12.5	12.68, 18.25	12.96, 12.68, 18.00
	8	25	12.5	12.68, 19.20	12.96, 12.68, 18.50

[a] Concentration of S vacancies (%) in the supercells (64 S sites).
[b] Lattice constant a of the 2H unit cell can be calculated as a/4, which is 3.16 Å.
[c] Lattice constants a and b of the 1T' unit cell can be calculated as a/2 and b/4. The angle between the a and b axes was 119°.
[d] The numbers of S mono-vacancies in the supercells (64 S sites).

Table S7. Parameters of (4×4) MoS_2-$m$$NH_4$ and (4×4) MoS_2-$m$$CH_3NH_3$ complexes in the 2H and 1T' phase for various concentration (C) of NH_4 and CH_3NH_3.

Guest	m	C (%)[a]	Phase[b]	E_{rel} (eV)[c]	E_{ic} (eV)[d]		ΔQ (e)[e]	
					2H	1T'	2H	1T'
None	0	0	2H	18.47	0	0	0	0
A (NH_4)	2	6.25	2H	13.13	1.44	-1.12	0.81	0.71
	4	12.5	2H	10.58	-0.01	-1.98	1.45	1.39
	6	18.75	2H	7.38	-0.58	-2.41	2.16	2.11
	8	25	2H	3.36	-0.82	-2.70	2.37	2.69
	10	31.25	2H	0.26	-0.90	-2.70	3.51	3.56
	12	37.5	1T'	-2.80	-0.92	-2.72	3.88	4.02
MA (CH_3NH_3)	2	6.25	2H	13.54	1.01	-1.45	0.79	0.76
	4	12.5	2H	11.27	-0.63	-2.51	1.56	1.65
	6	18.75	2H	7.51	-1.28	-3.10	2.39	2.40
	8	25	2H	5.32	-1.55	-3.15	3.20	3.49
	10	31.25	2H	1.35	-1.58	-3.23	3.57	3.60
	12	37.5	1T'	-0.61	-1.60	-3.26	3.64	3.52
None (C_{Vs}= 12.5)[f]	0	0	2H	9.51	0	0	0	0
MA (C_{Vs}= 12.5)[f]	2	6.25	2H	7.57	-0.78	-1.55	0.78	0.76
	4	12.5	2H	5.45	-1.89	-2.65	1.48	1.60
	6	18.75	2H	3.79	-2.24	-3.03	2.29	2.36
	8	25	1T'	-1.27	-2.32	-3.54	3.12	3.39

[a] Concentration of NH_4 and CH_3NH_3: [A]/[MoS_2] or [MA]/[MoS_2].
[b] Most stable phase among 2H and 1T'.
[c] Relative energy of the 1T' phase with respect to that of the 2H phase, i.e., E_{tot}(1T')-E_{tot}(2H). Positive and negative E_{rel} values denote that 2H and 1T' is the stable phase, respectively
[d] Intercalation energy per NH_4 or CH_3NH_3.
[e] Total charge transfer from m/2 NH_4 or CH_3NH_3 to a MoS_2 layer. As shown in Figure S15, the amount of total charge transfer was defined as $\Delta Q = Q_{max} - Q_{min}$, where Q_{max} and Q_{min} correspond to the maximum and minimum charge values in the regions adjacent to the MoS_2 layers and NH_4 (or CH_3NH_3), respectively. The average ΔQ value of (4×4) MoS_2-$m$$CH_3NH_3$ is larger than that of the (4×4) MoS_2-$m$$NH_4$; 0.35$e$ vs. 0.38e. The ΔQ value of the 2H and 1T' phase is nearly the same in both complexes.
[f] Concentration of S vacancies (%) is 12.5%, where the numbers of S mono-vacancies in the supercells (64 S sites) were N_{Vs} = 8.

Table S8. Closest distance of N-N (l_{N-N}) of (4×4) MoS_2-$m$$NH_4$ and (4×4) MoS_2-$m$$CH_3NH_3$ complexes in the 2H and 1T' phase for various concentrations (C) of NH_4 and CH_3NH_3.

Guest	m	C (%)[a]	2H		1T'	
			l_{N-N} (Å)	$\langle l_{N-N} \rangle$ [a]	l_{N-N} (Å)	$\langle l_{N-N} \rangle$ [a]
A (NH_4)	4	12.5	5.0, 5.0	5.00	4.12, 6.29	5.20
	6	18.75	4.34, 4.47, 4,47, 4.50	4.44	4.97, 4.16, 3.84, 6.14	4.77
	8	25	4.26, 4.18, 4.18, 4.33, 4.29	4.24	4.54, 3.54, 5.46, 3.69, 5.70	4.58
	10	31.25	3.70, 5.06, 4.31, 4.28, 3.53, 4.13	4.16	4.52, 4.18, 4.07, 4.20, 4.63, 4.50	4.35
	12	37.5	4.20, 4.19, 4.28, 4.04, 3.83, 4.25 ,3.93, 4.29, 4.50, 4.60, 4.14, 3.84	4.17	4.36, 4.04, 4.42, 3.79, 4.72, 4.84, 4.63, 4.26, 4.41, 4.46, 4.16, 4.24	4.35
MA (CH_3NH_3)	4	12.5	6.85, 5.50	6.17	6.78, 6.33	6.55
	6	18.75	5.57, 5.72, 5.54, 5.67, 6.04, 6.10	5.77	5.44, 5.52, 5.80, 6.11, 6.0, 6.18	5.69
	8	25	5.34, 5.24, 4.24, 4.38,4.20, 5.26, 5.37, 5.25	4.91	5.27, 4.93, 5.31, 4.77, 5.41, 4.89, 4.93, 4.56	5.0
	10	31.25	4.44, 4.43, 4.97, 4.48, 5.75, 5.71, 4.77, 4.45, 5.04, 5.00, 4.19	4.83	4.50, 5.47, 4.85, 5.19, 4.55,5.69, 4.69, 4.36, 4.63, 4.70, 5.25	4.89
	12	37.5	4.13, 4.44, 4.12, 4.84, 4.43, 4.49, 4.53, 4.95, 4.41, 4.68, 4.20, 4.04	4.43	4.24, 5.27, 5.52, 4.62, 4.84, 4.14, 4.67, 5.04, 5.12, 4.63, 4.74, 4.41	4.77
MA(C_{Vs}=12.5%)	4	12.5	5.13, 5.07	5.10	6.16, 5.14	5.65
	6	18.75	4.27, 4.74, 5.01, 5.03	4.76	4.64, 5.09, 5.45, 5.29	5.11
	8	25	4.34, 4.87, 4.96, 4.41, 4.70	4.65	4.35, 4.99, 4.88, 4.69, 4.89	4.76

[a] Average values.

III. Supporting Figures

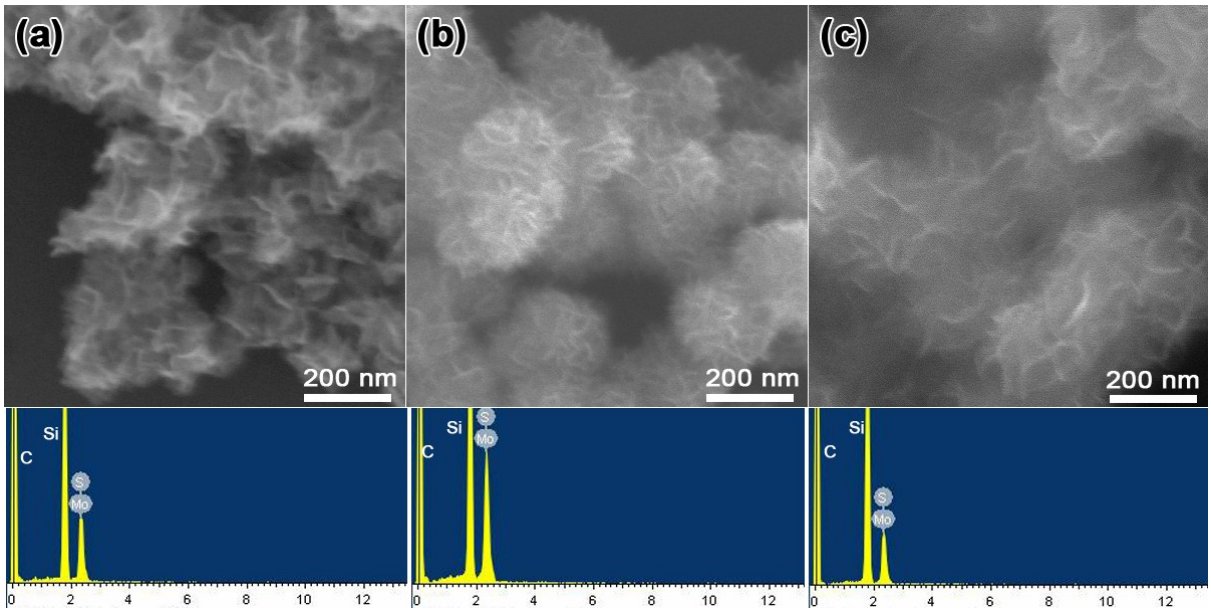

Fig. S1 Scanning electron microscopy images of (a) MS-0, (b) MS-A, and (c) MS-MA, and energy-dispersive X-ray fluorescence spectroscopy data.

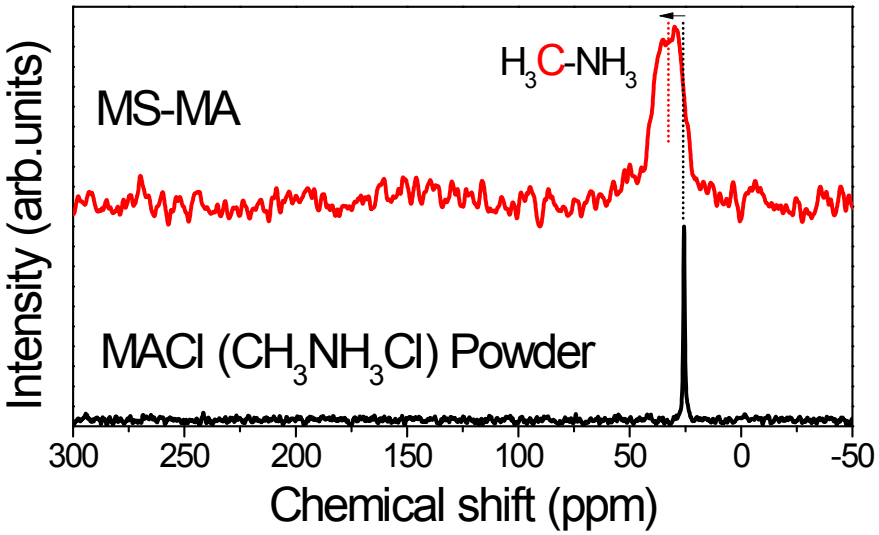

Fig. S2 ^{13}C NMR spectra of MACl powder and MS-MA. The MACl powder shows the CH_3 peak at 25.64 ppm. For MS-MA, the peak is relatively blue shifted (34.74 ppm), providing an evidence for the electron transfer to the MoS_2.

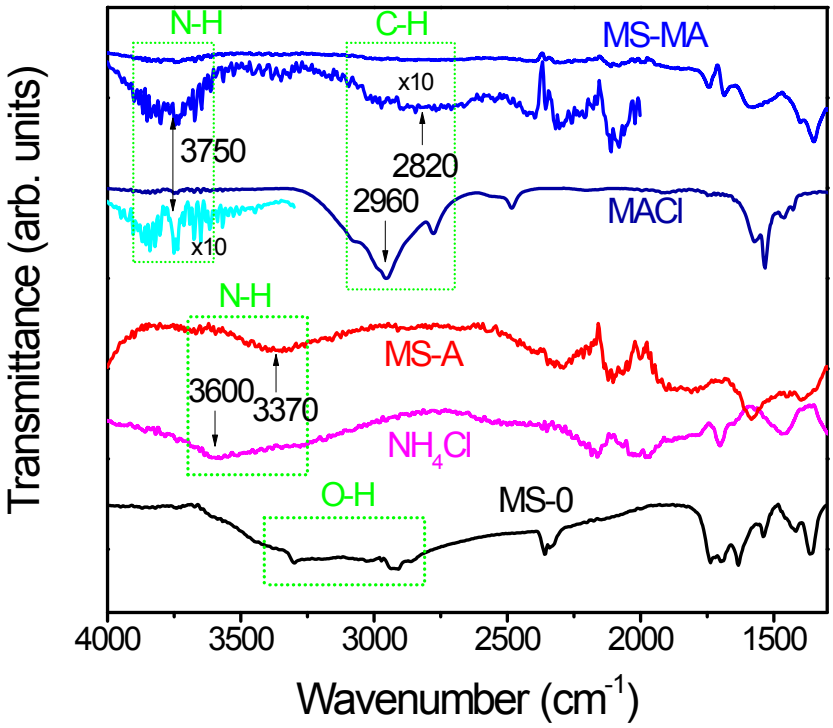

Fig. S3 IR spectra of MS-0, MS-A, and MS-MA, with those of NH_4Cl and MACl powders. MS-0 shows a broad O-H stretching vibrational mode at 2800-3400 cm^{-1}, due to the intercalated or adsorbed water.[S22] NH_4Cl and MS-A show the N-H stretching vibrational modes in the wide range of 3250-3700 cm^{-1}, suggesting the intercalation of NH_4 into the MoS_2. Both MACl and MS-MA show the N-H stretching vibrational modes at 3600-3900 cm^{-1} and the C-H stretching vibrational modes at 2700-3100 cm^{-1}, suggesting the intercalation of MA into MoS_2.

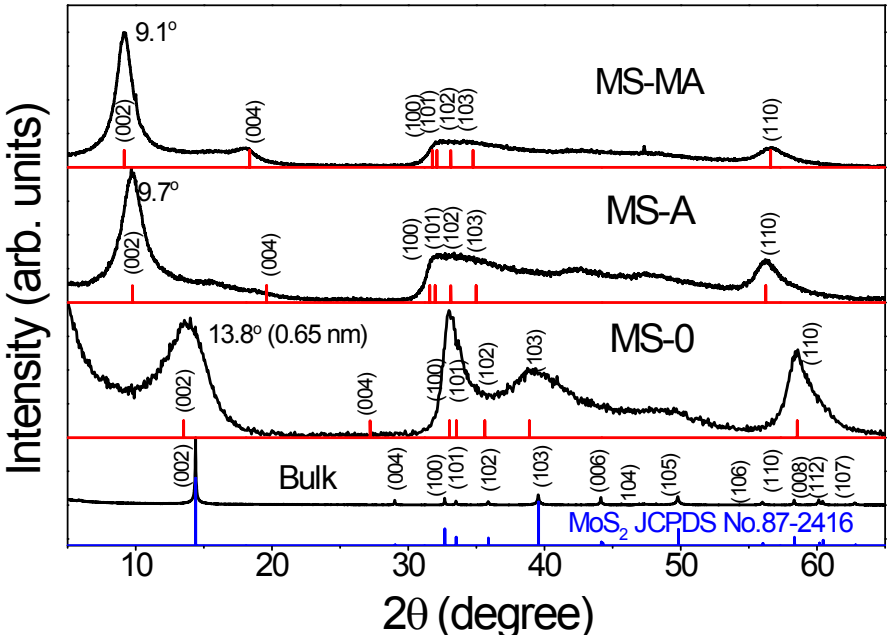

Fig. S4 XRD pattern of MS-0, MS-A, and MS-MA. The peaks were referenced to those of 2H phase MoS_2, shown at the bottom (JCPDS No. 87-2416; a = 3.160 Å and c = 12.290 Å).

The peaks of all samples were referenced to those of the hexagonal (2H) phase of bulk MoS_2 (JCPDS No. 87-2416; a = 3.160 Å and c = 12.290 Å). In the case of MS-0, the (002) peak at 2θ = 13.8° corresponds to a distance between (002) planes (d_{002}) of 6.5 Å (calculated using Bragg's law). This value is larger than that of 2H-MoS_2 (6.15 Å), probably due to the intercalation of water and ammonium ions that originated from the precursors. The (110) peak is located at 2θ = 58.6°, indicating the lattice constant a = 3.16 Å.

On the other hand, the (002) peaks of MS-A and MA-MS are shifted to lower 2θ angles of 9.7° and 9.1°, respectively, The intercalation of A and MA leads to a significant increase of the d_{002} value to 9.05 and 9.65 Å, respectively. The (110) peaks are also shifted to lower 2θ angles of 56.3° and 56.6°, respectively. The lattice constant a is estimated to be 3.27 and 3.26 Å, respectively, which is consistent with that (3.27 Å) of the distorted 1T (1T') phase.[S23]

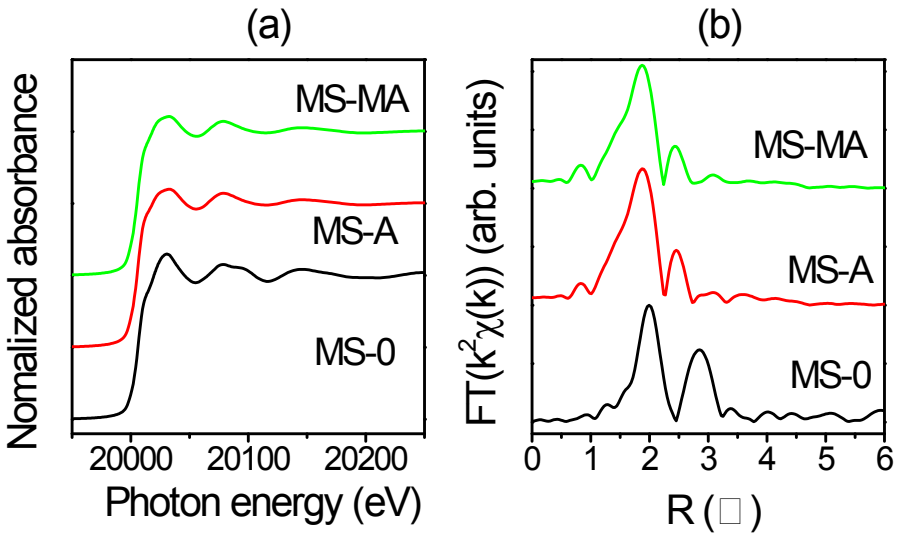

Fig. S5 (a) XANES and (b) EXAFS spectra at the Mo K edge for MS-0, MS-A, and MS-MA.

The evolution of the local crystal structure of MoS_2 upon the intercalation was probed with Mo K-edge X-ray absorption near edge spectra (XANES) analysis. In the Fourier transform (FT) profiles (in real space) of the extended X-ray absorption fine structure (EXAFS) above the Mo K-edge, the peaks indicate the distances to nearest neighbor atoms. The profiles of the MS-A and MS-MA are significantly different from that of MS-0, suggesting a remarkable change in the local atomic arrangements. The FT curves were fitted to two scattering shells. The fitting parameters are summarized in the Table S2. A least-squares curve parameter method was performed using the ARTEMIS module of IFEFFIT and USTCXAFS software packages.

The FT curves of the 2H phase MS-0 are characterized by two main peaks at 2.40 and 3.16 Å, corresponding to the nearest Mo–S and Mo–Mo bonds, respectively.[S24,S25] In contrast, in the FT curves of MS-A and MS-MA, the second peak (related to the nearest Mo–Mo bond) shows a noticeable shift from 3.16 to 2.76 Å. The intensity of this peak is nearly reduced by half, corresponding to the coordination number of Mo-Mo decreased by almost half. All these results indicate that the intercalated MoS_2 adopts a distorted octahedral coordination. The Debye-Waller factor, which measure the static and thermal disorder, is larger for MS-A and MS-MA than MS-0. It suggests that the intercalation produces a broad range of Mo-S and Mo-Mo distances.

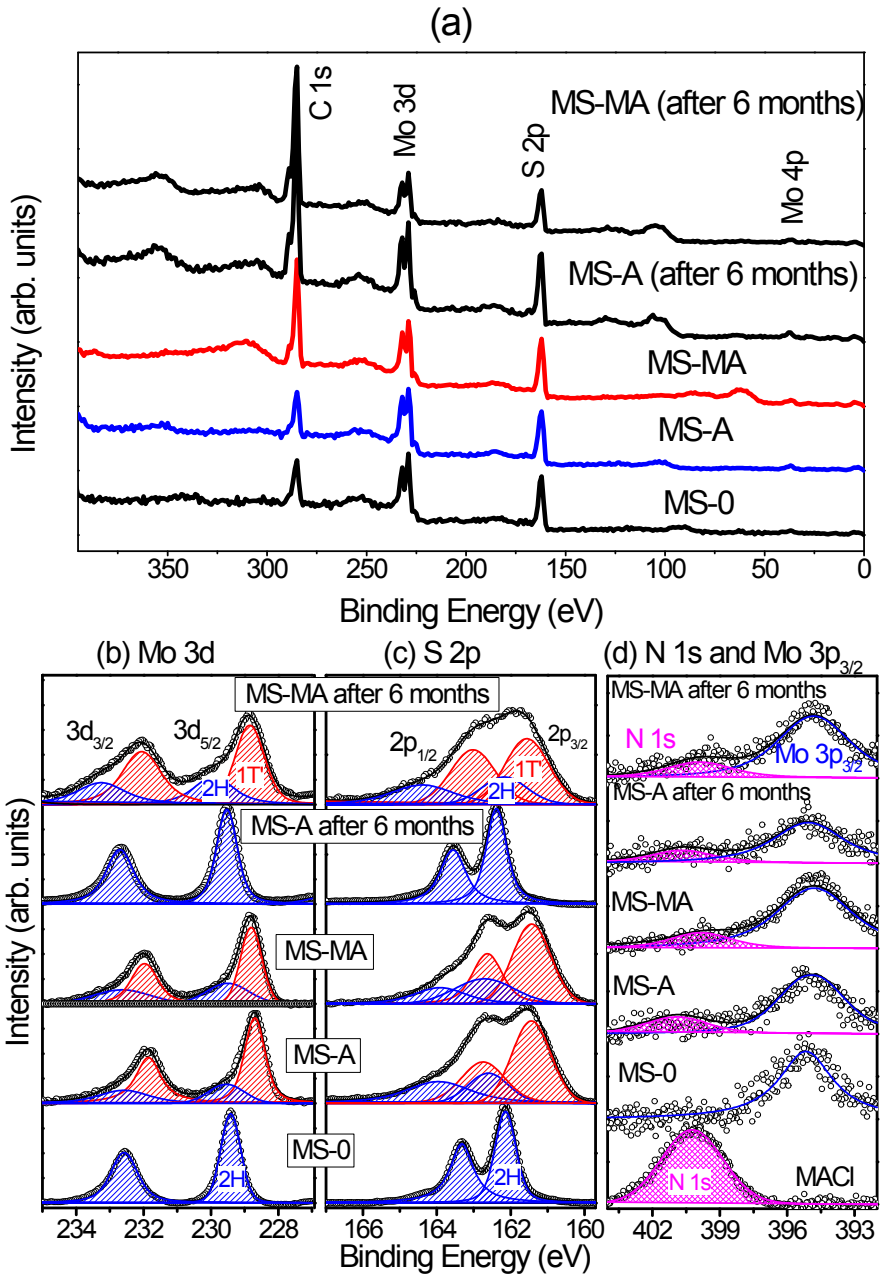

Fig. S6 (a) XPS survey scans of MS-0, MS-A, and MS-MA samples before and after 6 months of storage under ambient condition. Fine-scanned XPS (b) Mo 3d, (c) S 2p, and (d) N 1s and Mo $3p_{3/2}$ peaks. The XPS data (open circles) are fitted by Voigt functions, and the sum of the resolved bands is represented by black lines.

The survey scan of MS-0, MS-A, and MS-MA is shown in Figure S5a. The C peak is larger for MS-MA compared to that of others, due to the methyl group. The fine-scanned Mo 3d peak is shown in Figure S5b. After 6 months, the 1T' phase of MS-A was converted to the 2H phase afterwards. In contrast, the 1T' phase of MS-MA persisted. Figure S5c shows the S $2p_{3/2}$ and $2p_{1/2}$ peaks that are separated by about 2 eV. MS-0 show peaks at 162.1 and 163.3 eV, which are redshifted by 1.9 eV with respect to those of neutral S (S^0) at 164.0 and 165.2 eV, and correspond to the S^{2-} anions bonded with the Mo cations of the 2H phase. For MS-A and MS-MA, the broad peak was resolved into four bands; two for the 2H phase (blue) and two for the 1T' phase (red). The 2H- and 1T'-phase bands show 1.5 and 2.6 eV of red shift relative to S^0, respectively. The larger red shift is ascribed to the electron-rich S ions of the 1T' phase. After 6 months, MS-MA still shows the 1T' phase peak, but MS-A shows the 2H phase peak.

Figure S5d shows the N 1s and Mo $3p_{3/2}$ peaks (at 395 eV). The N 1s peak of MACl powders, MS-A, and MS-MA appears at 400-401 eV, and is blue shifted with respect to that of neutral N (N^0) at 398.1 eV. This indicates that the intercalated A and MA have positively charged.

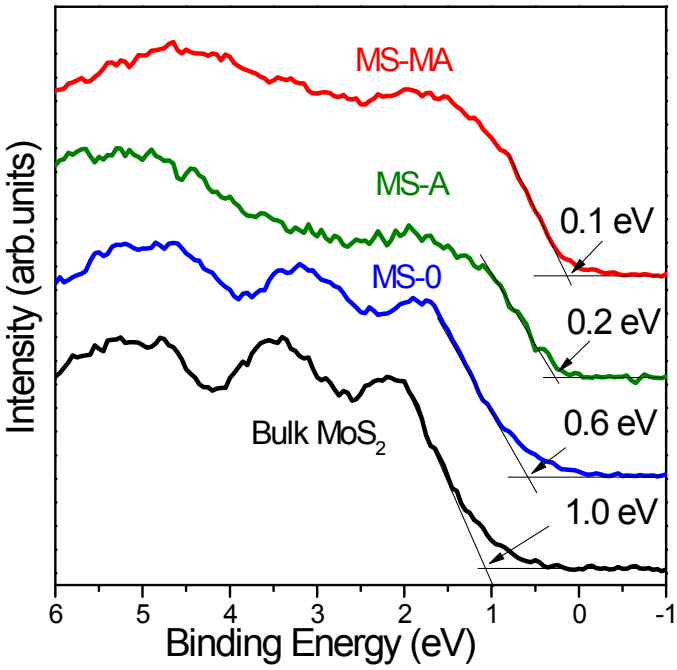

Fig. S7 XPS valence band spectra of bulk MoS_2 (powders) and MS samples (MS-0, MS-A, and MS-MA), showing the valence band position.

The positions of the valence band maximum (VBM) were evaluated by linear extrapolation of the onset in the XPS valence band (VB) spectra. The zero-binding energy was calibrated using the work function of Au metal. The VBM value of the 2H phase bulk MoS_2 and MS-0 is 1.0 and 0.6 eV, respectively. As the A and MA were intercalated, the VBM was redshifted to 0.2 and 0.1 eV, respectively, which supports the production of the metallic 1T' phase.

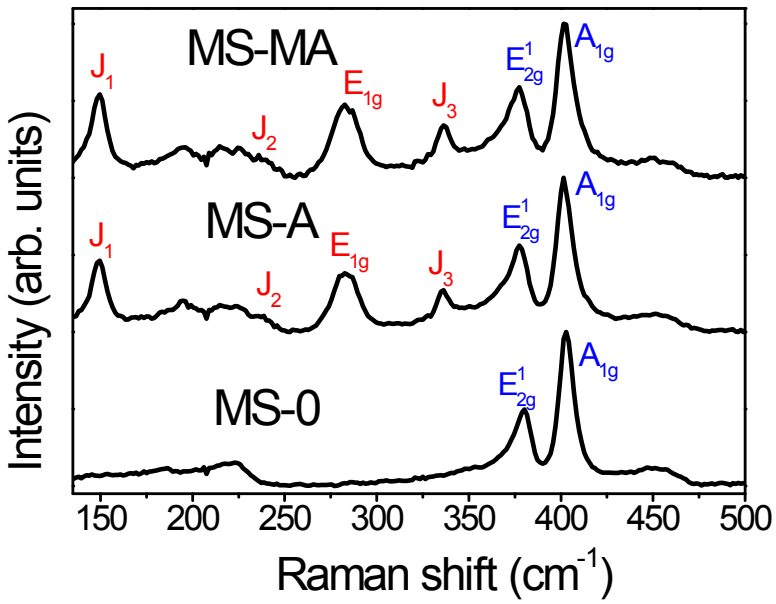

Fig. S8 Raman spectrum of MS-0, MS-A, and MS-MA samples. Excitation laser is 532 nm diode laser.

The MS-0 exhibit the characteristic Raman peaks of the 2H phase at 380 and 403 cm^{-1} corresponding to the in-plane E^1_{2g} and out-of-plane A_{1g} vibration modes, respectively. The Raman spectra of MS-A and MS-MA show three typical peaks of the distorted 1T' phase: the J_1 peak at 148 cm^{-1}, the J_2 peak at 236 cm^{-1}, and the J_3 peak at 336 cm^{-1}.[S26] The E_g vibration mode peak appears at 284 cm^{-1}. Therefore, the intercalated samples consisted of the 1T' phase.

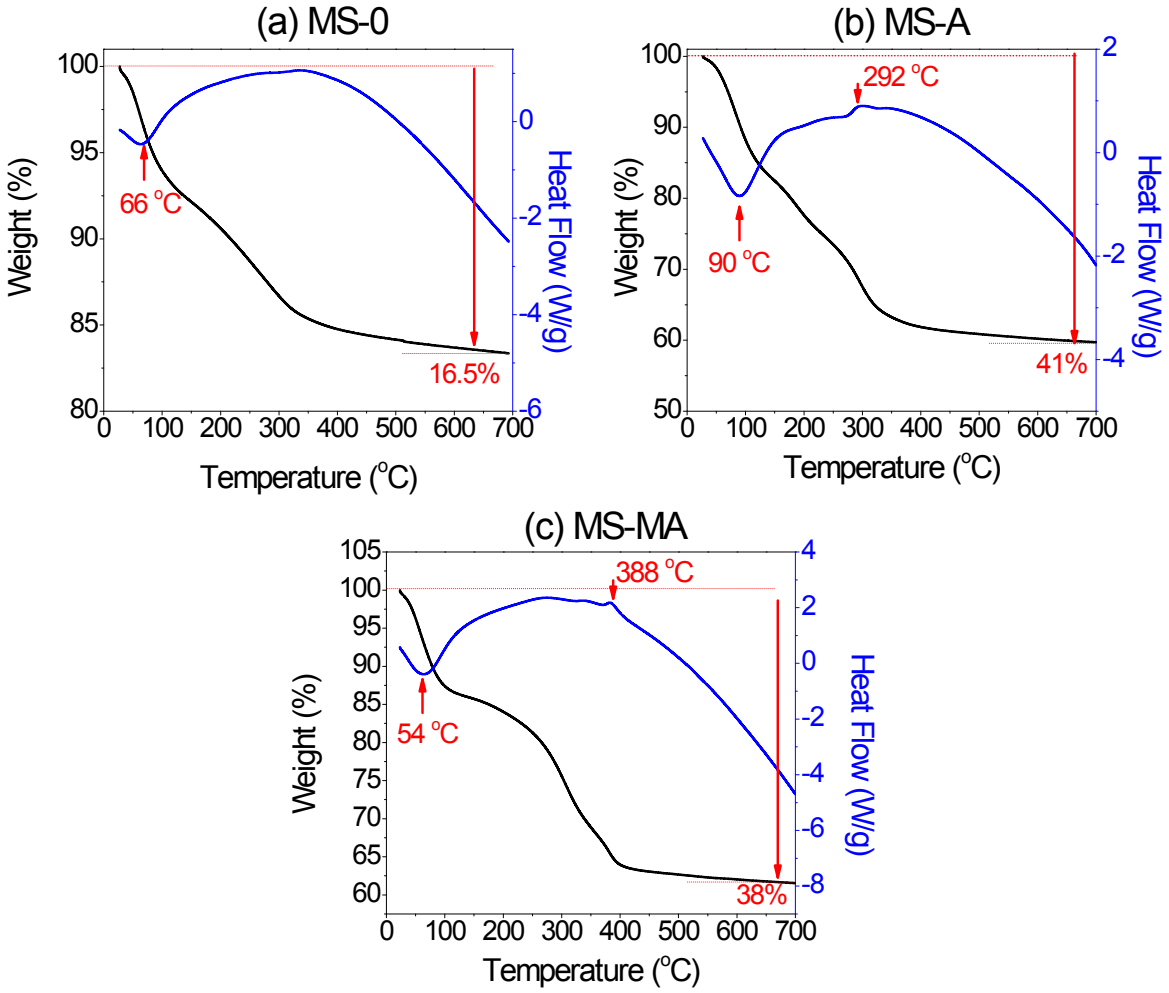

Fig. S9 TGA and DSC data of (a) MS-0, (b) MS-A, and (c) MS-MA. The samples were heated from room temperature to 700 °C at 10 °C/min and under N_2 flow (100 sccm).

Thermogravimetric analysis (TGA) curve of MS-0 shows a total loss of 16.5% at 700 °C, which can be divided into the partial losses of 6% at 25–100 °C, 9% at 100–340 °C, and 1.5% between 340 and 700 °C. The differential scanning calorimetry (DSC) curve shows an endothermic peak at 66 °C, corresponding to the first weight loss step, which is ascribed to the release of adsorbed species such as water. The second weight loss of 10% is probably due to the intercalated water and ammonium ions that originated from the precursors.

MS-A shows 16% weight losses in the 25-130 °C range, 17% at 130-350 °C, and 8% between 350 and 700 °C, with a total weight loss of 41%. The DSC curve shows an

endothermic peak at 90 °C corresponding to the release of adsorbates. An exothermic peak, not observed for MS-0, emerges at 292 °C. This peak could be due to the transition from the 1T' to the 2H phase.[S7]

The TGA curve of MS-MA shows a total weight loss of 38% at 700 °C, which can be divided into partial losses of 13% at 25–100 °C, 23% at 100–400 °C, and 2% between 400 and 700 °C. The DSC curve shows an endothermic peak at 54 °C, and an exothermic peak at 388 °C, corresponding to the release of adsorbates and the 1T' $\rightarrow$ 2H transition, respectively. The higher phase transition temperature than that observed in MS-A is correlated with the higher stability of the 1T' phase.

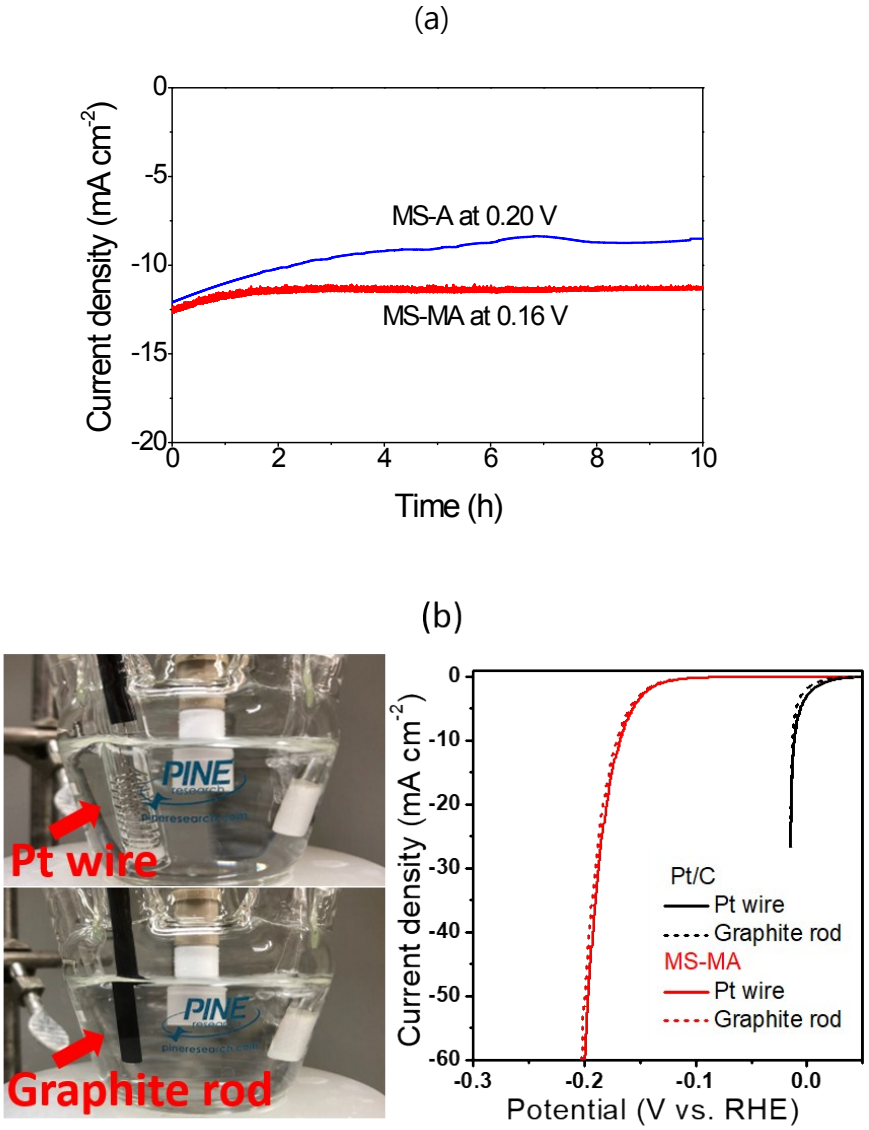

Fig. S10 (a) Chronoamperometric responses of MS-A (at 0.20 V) and MS-MA (at 0.16 V), showing the respective current attenuation of 25% and 5% after 10 h. (b) LSV curves (scan rate: 2 mV s^{-1}) using the graphite rod as a counter electrode. The Photograph (left) show the cell set up when the Pt wire and graphite rod were used as counter electrode. The Pt wire counter electrode was shielded by a membrane that block the transmission of the dissolved Pt ions into the electrolyte. Since the Pt ions did not contaminate the electrolyte, no Pt deposition on the working GC electrode would occur.

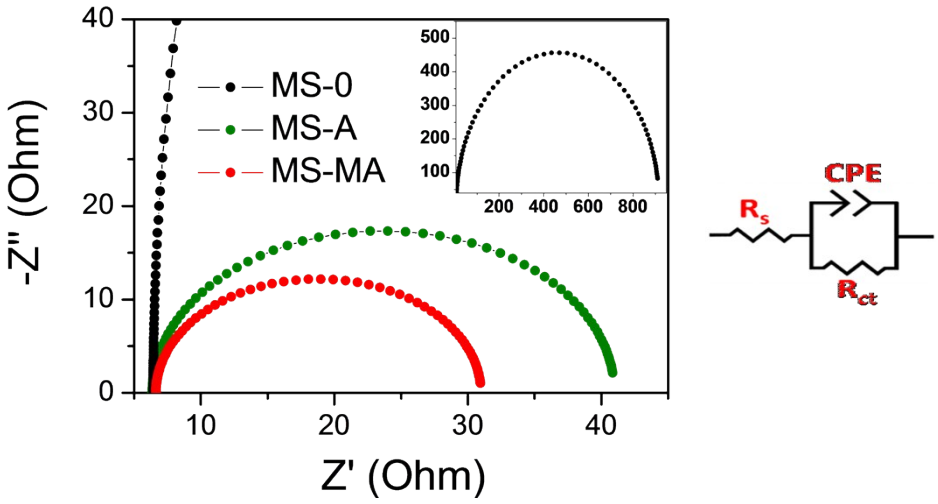

Fig. S11 Nyquist plots for EIS measurements from 100 kHz to 0.1 Hz at a representative potential of -0.15 V (vs. RHE) and the equivalent circuit diagram.

Electrochemical impedance spectroscopy (EIS) measurements were performed in the frequency range of 100 kHz–0.1 Hz and an amplitude of 10 mV at η = 0.15 V. In the high-frequency limit and under non-Faradaic conditions, the electrochemical system is approximated by the modified Randles circuit shown on the right of Figure S11, where R_s denotes the solution resistance, CPE is a constant-phase element related to the double-layer capacitance, and R_{ct} is the charge-transfer resistance from any residual Faradaic processes. A semicircle in the low-frequency region of the Nyquist plots represents the charge transfer process, with the diameter of the semicircle reflecting the charge-transfer resistance. The real (Z') and negative imaginary ($-Z''$) components of the impedance are plotted on the x and y axes, respectively. Simulating the EIS spectra using an equivalent circuit model allowed us to determine R_{ct}, which is a key parameter for characterizing the catalyst-electrolyte charge transfer process. The fitting parameters are listed in Table S3.

The obtained R_{ct} values are 910.8, 40.9, and 32.7 Ω for MS-0, MS-A, and MS-MA, respectively. The intercalated samples have much smaller charge transfer resistance (R_{ct}) than MS-0. The order of R_{ct} is consistent with that of the HER performance. The reduced charge-transfer resistance plays a major role in enhancing the HER catalytic activity of the intercalated samples.

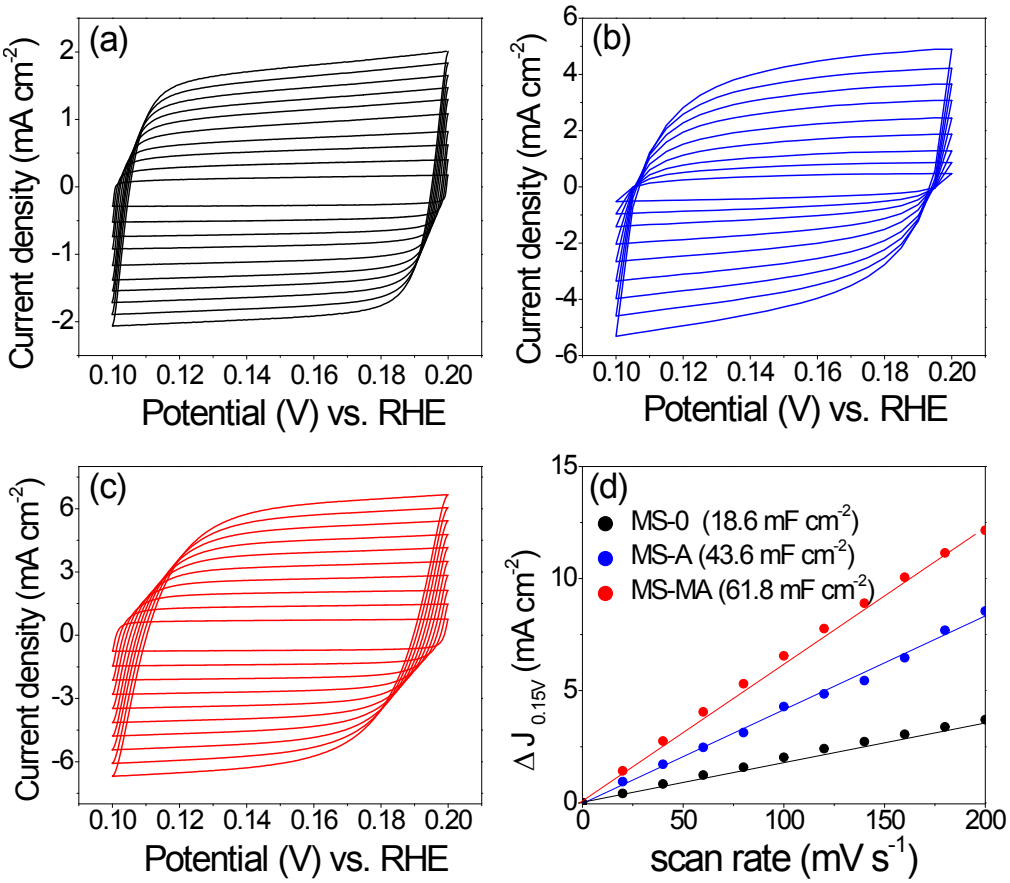

Fig. S12 Cyclic voltammograms of (a) MS-0, (b) MS-A, and (c) MS-MA in a non-Faradaic region (0.1-0.2 V vs. RHE), at 20–200 mV s^{-1} scan rates and in 0.5 M H_2SO_4 solution. (d) Difference (ΔJ) between the anodic charging and cathodic discharging currents measured at 0.15 V (vs. RHE) and plotted as a function of the scan rate.

Cyclic voltammograms were measured at 0.1-0.2 V, in a non-Faradaic region, using various scan rates. The double-layer capacitance (C_{dl}) was obtained as the slope of a linear fit of ΔJ vs. scan rate, where ΔJ is the difference between the anodic charging (positive value) and cathodic discharging currents (positive value). The C_{dl} values of MS-0, MS-A, and MS-MA are 18.6, 43.6, and 61.8 mF cm^{-2}, respectively (see the summary in Table S3), showing a significant increase upon intercalation. The intercalated MoS_2 samples have very rough surfaces and can thus expose a large number of active sites. Therefore, the increased double-layer capacitance leads to the enhanced HER catalytic activity of the intercalated samples. The C_{dl} values follow the same order as that of HER performance: MS-MA > MS-A > MS-0.

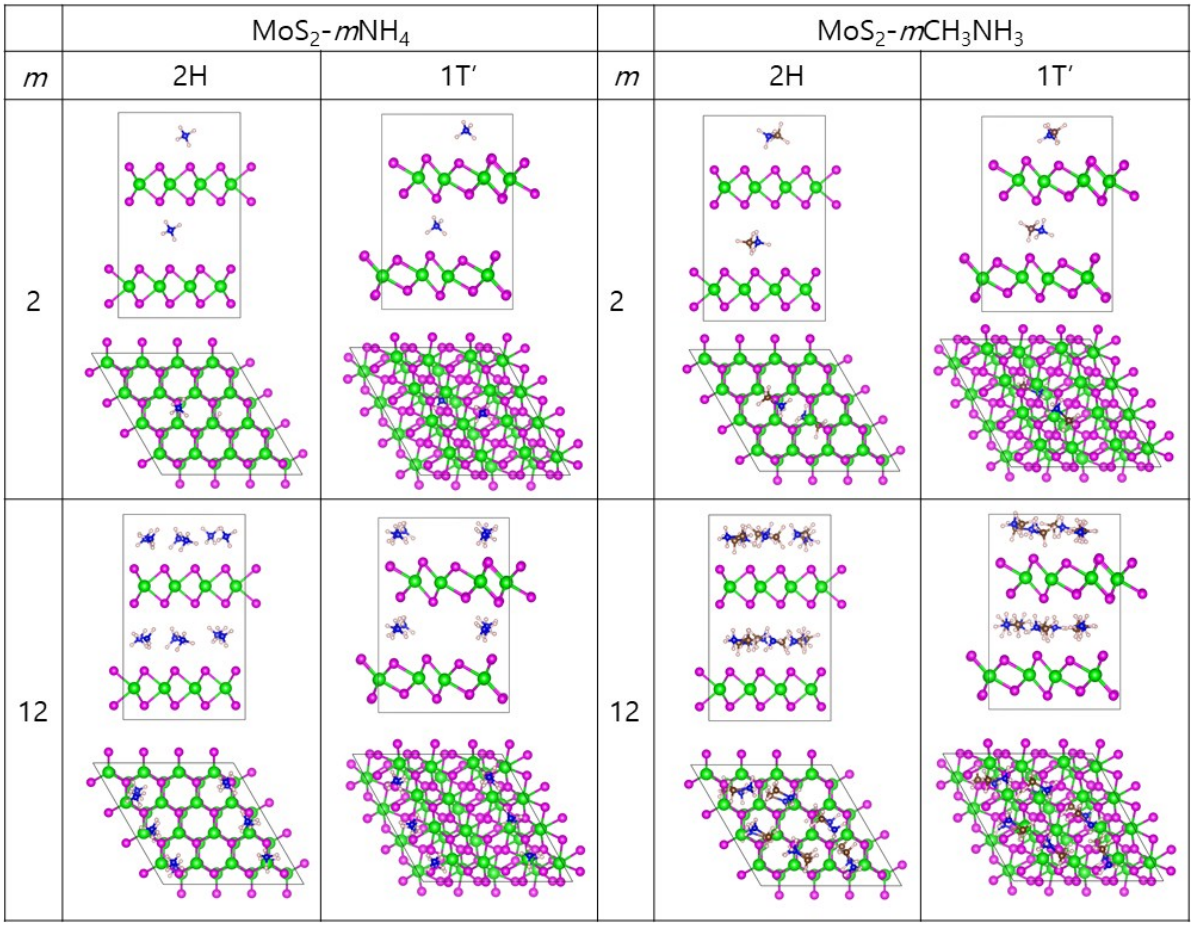

Fig. S13 Structures of the 2H and 1T' phases (4×4) MoS_2-$m$$NH_4$ and (4×4) MoS_2-$m$$CH_3NH_3$ (m = 2 and 12).

In the theoretical calculation, the NH_4 or CH_3NH_3 radicals are placed in such a way that they have inversion symmetry with respect to other NH_4. The (4×4) MoS_2-$m$$CH_3NH_3$ complex can adopt two different configurations for the two CH_3NH_3 moieties: head-to-head (HH, CH_3NH_3···NH_3CH_3) and head-to-tail (HT, CH_3NH_3···CH_3NH_3). To compare the two configurations, the guest concentration has to be at least C = 12.5% (m = 4), where two CH_3NH_3 moieties are present between a pair of MoS_2 layers in a supercell. At this concentration, the HH configuration is more stable than HT by 0.10 and 0.30 eV for the 1T' and 2H phases, respectively. This observation can be understood by noting that most of the positive charge in the $CH_3NH_3^+$ ion is carried by the NH_3 group instead of CH_3, so that the electrostatic repulsion

between the pair is weaker in the HH configuration. At higher concentrations, the most stable configuration should be the one that maximizes the number of HH pairs. For MoS_2-8CH_3NH_3 (C = 25%), we find that the configuration (HHa) in which all pairs follow the HH orientation is much more stable (by 1.50 and 0.98 eV for 2H and 1T' phases, respectively) than that (HTa) in which no pairs have the HH configuration.

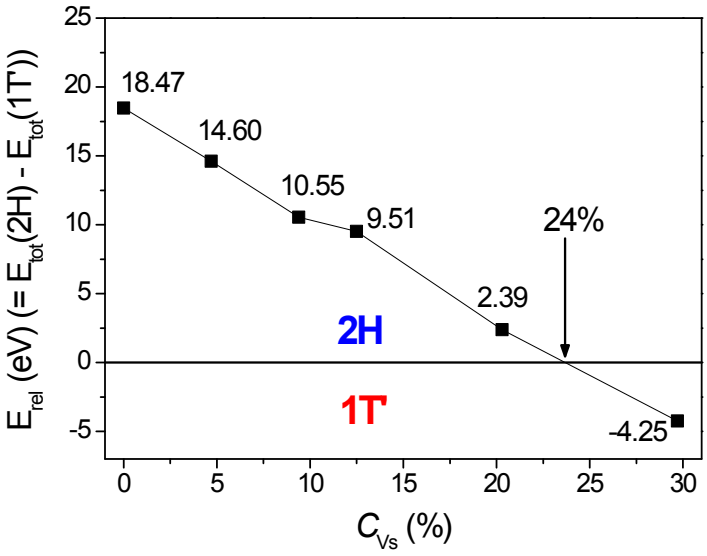

Fig. S14 Relative energy (E_{rel}) of the 1T' and 2H phases (4×4) MoS_2 at C_{Vs} = 0, 4.7, 9.4, 12.5, 20.3, and 29.7%. The E_{rel} as a function of C_{Vs} for non-intercalated MoS_2 shows the 2H → 1T' phase transition at C_{Vs} = 24%. It indicates that the S vacancies increased the electron density that favors the 1T' phase.

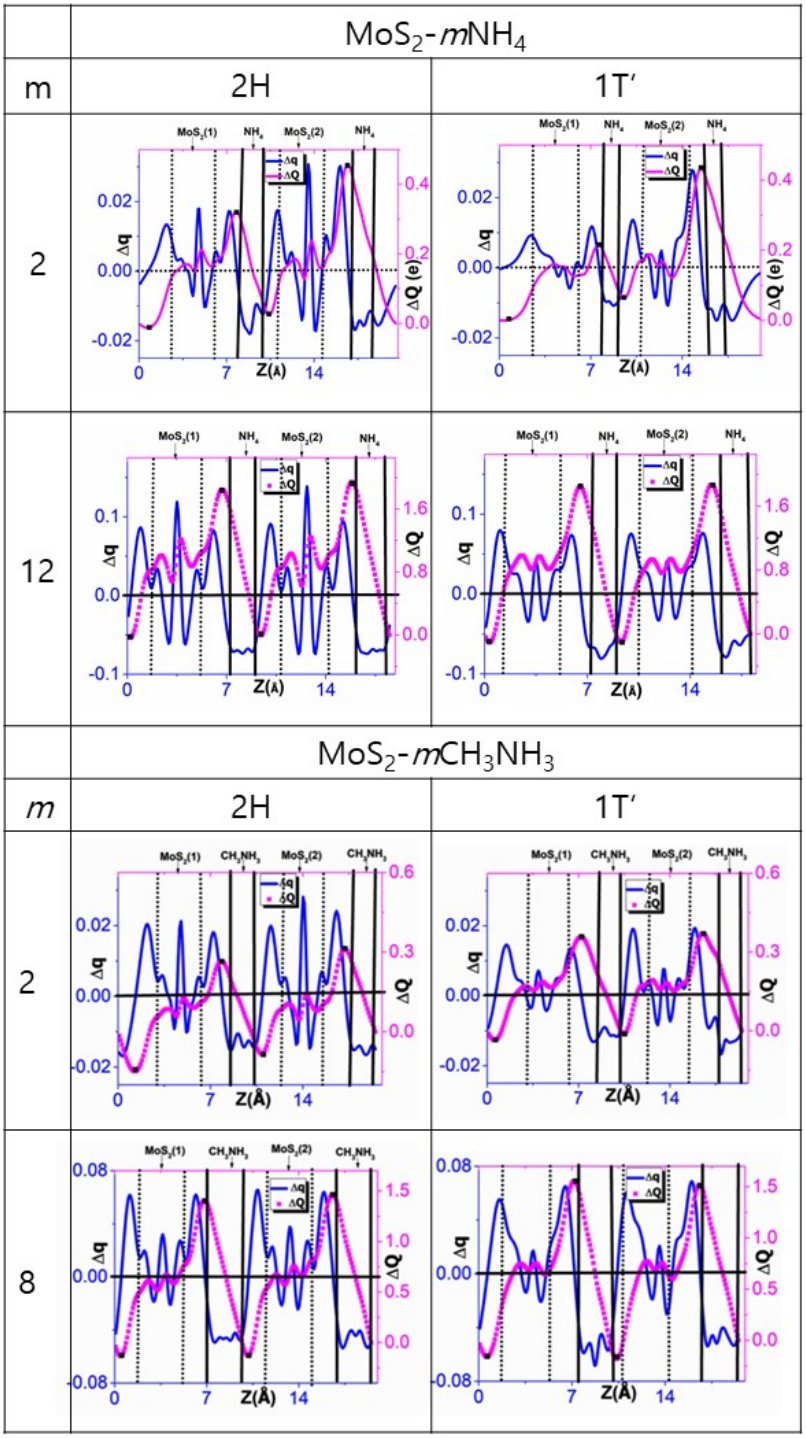

Fig. S15 $\Delta q(z)$ (blue line, left axis) and $\Delta Q(z)$ (pink line, right axis) of (4×4) MoS_2-$m$$NH_4$ (m = 2 and 12) and (4×4) MoS_2-$m$$CH_3NH_3$ (m = 2 and 8 with C_{Vs}= 12.5%) in the 2H and 1T' phases.

The change in electron density (expressed in e Å^{-3}) along the c (*i.e., z*) axis generated by the intercalation process of NH_4 (A) or CH_3NH_3 (MA) was defined as $\Delta\rho(z) = \rho(z)[MoS_2\text{-}m\text{A}] - \rho(z)[MoS_2] - \rho(z)[m\text{A}]$ or $\Delta\rho(z) = \rho(z)[MoS_2\text{-}m\text{MA}] - \rho(z)[MoS_2] - \rho(z)[m\text{MA}]$, averaged over the *xy* plane in a supercell. The total electron density change (e) was defined as $\Delta q(z) = \Delta\rho(z)\Delta V$, where ΔV is the volume of a fine grid, i.e., $\Delta V = V_{cell}/N_c$, in which V_{cell} is the total volume of the supercell and N_c = 1–200 is the number of fine grids. The thickness of each MoS_2 layer was defined on the basis of the z coordinates of the S atoms in the upper and lower sublayers (S_L and S_U), with $z(S_L) < z(S_U)$. The size of A or MA between a specific pair of MoS_2 layers is defined by the minimum and maximum of z coordinates of all atoms.

The $Q(z)$, displayed on the right y-axis, represents the accumulated excess charge in the interval $[0, z]$: $Q(z) = \sum_{0}^{z'<z} \Delta q(z')$. The amount of charge transfer was defined as $\Delta Q = Q_{max} - Q_{min}$, where Q_{max} and Q_{min} correspond to the maximum and minimum charge values in the regions adjacent to the MoS_2 layers and A (or MA), respectively. The z values corresponding to $Q_{min}(z)$ and $Q_{max}(z)$ are shown by filled squares. A significant decrease of $\Delta q(z)$ for A or MA signals the conversion of the radical to the positively charged ion. The ΔQ value increases with increasing concentration of A or MA.

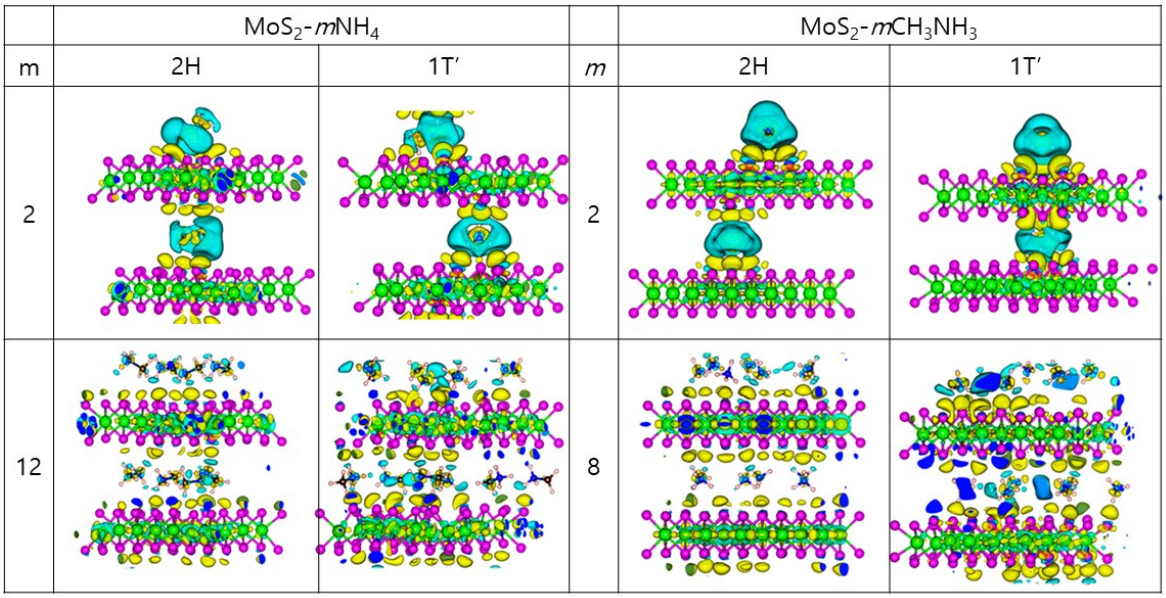

Fig. S16 Contour plots of $\Delta\rho(x, y, z)$ of the 2H and 1T' phase (4×4) MoS_2-$m$$NH_4$ (m = 2 and 12) and (4×4) MoS_2-$m$$CH_3NH_3$ (m = 2 and 8) with C_{Vs}= 12.5%. Charge accumulation and depletion are represented by yellow and turquoise colors, respectively. The plots reveal significant electron transfer from NH_4 (A) or CH_3NH_3 (MA) to the MoS_2 layer. The majority of the transferred electrons are concentrated on the interlayer region between the A (or MA) and the adjacent S atoms of MoS_2, suggesting a strong electrostatic interaction between the transferred electrons and the hydrogen atoms bonded to the nitrogen of A or MA.

IV. References

S1. T. P. Prasad, E. Diemann and A. Müller, *J. Inorg. Nucl. Chem.*,1973, **35**, 1895-1904.

S2. G. Kresse and J. Hafner, *Phys. Rev. B*, 1993, **47**, 558-561.

S3. G. Kresse and J. Furthmüller, *Phys. Rev. B*, 1996, **54**, 11169-11186.

S4. G. Kresse and D. Joubert, *Phys. Rev. B*, 1999, **59**, 1758-1775.

S5. S. Grimme, *Comput. Chem.*, 2006, **27**, 1787–1799.

S6. J. Xie, H. Zhang, S. Li, R. Wang, X. Sun, M. Zhou, J. Zhou, X. W. Lou and Y. Xie, *Adv. Mater.,* 2013*,* **25***,* 5807-5813.

S7. D. Voiry, M. Salehi, R. Silva, T. Fujita, M. Chen, T. Asefa, V. B. Shenoy, G. Eda and M. Chhowalla, *Nano Lett.,* 2013, **13**, 6222-6227.

S8. J. Xie, J. Zhang, S. Li, F. Grote, X. Zhang, H. Zhang, R. Wang, Y. Lei, B. Pan and Y. Xie, *J. Am. Chem. Soc.,* 2013, **135**, 17881-17888.

S9. M. Gao, M. K.Y. Chan and Y. Sun, *Nat. Commun.,* 2015, **6**, 7493.

S10. H. Li, C. Tsai, A. L. Koh, L. Cai, A. W. Contryman, A. H. Fragapane, J. Zhao, H. S. Han, H. C. Manoharan, F. A. Pedersen, J. K. Nørskov and X. Zheng, *Nat. Mater.,* 2015, **15**, 48-53.

S11. Z. Wu, C. Tang, P. Zhou, Z. Liu, Y. Xu, D. Wang and B. Fang, *J. Mater. Chem. A,* 2015, **3**, 13050-13056.

S12. D. Voiry, R. Fullon, J. Yang, C. C. C. Silva, R. Kappera, I. Bozkurt, D. Kaplan, M. J. Lagos, P. E. Batson, G. Gupta, A. D. Mohite, L. Dong, D. Er, V. B. Shenoy, T. Asefa and M. Chhowalla, *Nat. Mater.,* 2016*,* **15***,* 1003–1009.

S13. X. Geng, W. Sun, W. Wu, B. Chen, A. A. Hilo, M. Benamara, H. Zhu, F. Watanabe, J. Cui and T. Chen, *Nat. Commun.,* 2016, **7**, 10672.

S14. Y. Yin, J. Han, Y. Zhang, X. Zhang, P. Xu, Q. Yuan, L. Samad, X. Wang, Y. Wang, Z. Zhang, P. Zhang, X. Cao, B. Song and S. Jin, *J. Am. Chem. Soc.,* 2016, **138***,* 7965-7972.

S15. F. Z. Wang, M. J. Zheng, B. Zhang, C. Q. Zhu, Q. Li, L. Ma and W. Z. Shen, *Sci. Rep.,* 2016, **6***,* 31092.

S16. Y. Kim, D. H. K. Jackson, D. Lee, M. Choi, T. W. Kim, S. Y. Jeong, H. J. Chae, H. W. Kim, N. Park, H. Chang, T. F. Kuech and H. J. Kim, *Adv. Funct. Mater.,* 2017, **27**, 1701825.

S17. J. Zhang, J. Wu, H. Guo, W. Chen, J. Yuan, U. Martinez, G. Gupta, A. Mohite, P. M. Ajayan and J. Lou, *Adv. Mater.,* 2017*,* **29***,* 1701955.

S18. D. Wang, X. Zhang, S. Bao, Z. Zhang, H. Feia and Z. Wu, *J. Mater. Chem. A,* 2017, **5**, 2681–2688.

S19. Y. Shi, Y. Zhou, D. R. Yang, W. X. Xu, C. Wang, F. B. Wang, J. J. Xu, X. H. Xia and H. Y. Chen, *J. Am. Chem. Soc., 2017*, **139**, 15479-15485.

S20. E. E. Benson, H. Zhang, S. A. Schuman, S. U. Nanayakkara, N. D. Bronstein, S. Ferrere, J. L. Blackburn and E. M. Miller, *J. Am. Chem. Soc.,* 2018, **140***,* 441−450.

S21. C. Tan, Z. Luo, A. Chaturvedi, Y. Cai, Y. Du, Y. Gong, Y. Huang, Z. Lai, X. Zhang, L. Zheng, X. Qi, M. H. Goh, J. Wang, S. Han, X. Wu, L. Gu, C. Kloc and H. Zhang, *Adv. Mater*., 2018, **30***,* 1705509.

S22. K, Nakamoto, Infrared and Raman Spectra of Inorganic and Coordination Compound, 4th Ed. 1986, Jon Wiley & Sons.

S23. D. Yang, S. J. Sandoval, W. M. R. Divigalpitiya, J. C. Irwin and R. F. Frindt, *Phys. Rev. B*, 1991, **43**, 12053-12056.

S24. S. S. Chou, N. Sai, P. Lu, E. N. Coker, S. Liu, K. Artyushkova, T. S. Luk, B. Kaehr and C. J. Brinker, *Nat. Commun.*, 2015, **6**, 8311-8319.

S25. Q. Liu, X. Li, Q. He, A. Khalil, D. Liu, T. Xiang, X. Wu and L. Song, *Small*, 2015, **11***,* 5556–5564.

S26. S. J. Sandoval, D. Yang, R. F. Frindt and J. C. Irwin, *Phys. Rev. B*, 1991, **44**, 3955-3962.